

A STUDY OF THE DYNAMICS OF DUST FROM THE KUIPER BELT: SPATIAL DISTRIBUTION AND SPECTRAL ENERGY DISTRIBUTION

AMAYA MORO-MARTÍN¹ AND RENU MALHOTRA²

Received 2002 May 8; accepted 2002 July 9

ABSTRACT

The dust produced in the Kuiper belt (KB) spreads throughout the solar system, forming a dust disk. We numerically model the orbital evolution of KB dust and estimate its equilibrium spatial distribution and its brightness and spectral energy distribution (SED), assuming graybody absorption and emission by the dust grains. We show that the planets modify the KB disk SED, so potentially we can infer the presence of planets in spatially unresolved debris disks by studying the shape of their SEDs. We point out that there are inherent uncertainties in the prediction of structure in the dust disk, owing to the chaotic dynamics of dust orbital evolution imposed by resonant gravitational perturbations of the planets.

Key words: celestial mechanics — interplanetary medium — Kuiper belt —
 methods: n -body simulations — methods: numerical — planetary systems —
 solar system: general

1. INTRODUCTION

Main-sequence stars are commonly surrounded by cold material that emits in the far-infrared. The fact that this infrared excess is not restricted to young stars, and that the dust grain removal processes, Poynting-Robertson (P-R) effect, and solar wind drag, act on timescales much smaller than the age of the system, indicate that (1) a reservoir of undetected dust-producing planetesimals exists and (2) to induce frequent mutual collisions, their orbits must be dynamically perturbed by massive planetary bodies. The solar system is also filled with interplanetary dust. In the inner solar system, this dust, which gives rise to the zodiacal light, has been observed by *Pioneer 10* (out to 3.3 AU) and by the infrared telescopes *IRAS* and *COBE*. The dominant sources of the zodiacal cloud are debris from Jupiter-family short-period comets and asteroids (Liou, Dermott, & Xu 1995; Dermott et al. 1992). The discovery of a debris disk around β Pictoris, extending to hundreds of AU, together with the confirmation of the existence of the theoretically predicted Kuiper belt objects (KBOs; Jewitt & Luu 1995), suggest that significant dust production may also occur in the outer solar system as the result of mutual collisions of KBOs (Backman & Paresce 1993; Backman, Dasgupta, & Stencel 1995; Stern 1996) and collisions with interstellar grains (Yamamoto & Mukai 1998).

Dust particles are small enough to experience the effect of radiation and stellar wind forces. Radiation pressure makes their orbital elements and specific orbital energy change immediately upon release from their parent bodies. If their orbital energy becomes positive, the dust particles escape on hyperbolic orbits. In the solar system, these particles are known as β -meteoroids (Zook & Berg 1975). If their orbital energy remains negative, the dust particles stay on bound orbits. P-R and solar wind drag tends to circularize and

decrease the semimajor axes of these orbits, forcing these particles to slowly drift in toward the central star (Burns, Lamy, & Soter 1979). Assuming that the dust particles are constantly being produced, this drifting in creates a dust disk of wide radial extent, which we refer to as a “debris disk.” Debris disks are systems that satisfy the following conditions: (1) their age is longer than the P-R and collisional lifetimes, (2) they are optically thin to stellar radiation, even along the midplane, and (3) they have little or no gas so that the dust dynamics is controlled by gravitation and radiation forces only (D. E. Backman 2002, private communication).

When planets are present, the journey of a dust particle toward the central star is temporarily interrupted by trapping of the particle in mean motion resonances (MMRs). MMRs occur when the orbital period of the particle is in a ratio of small integers to that of the perturbing planet. (The $p:q$ MMR means that the orbital period of the particle is p/q times that of the planet.) In an MMR, the drifting in is halted because the energy loss due to P-R drag is balanced by the resonant interaction with the planet’s gravity field. This trapping can potentially create structure in debris disks, as the particles accumulate at certain semimajor axes. Sufficiently massive planets may also scatter and eject dust particles out of a planetary system, creating dust-free or depleted zones. This structure, if observed, can be used to infer the presence of planets. Liou & Zook (1999, hereafter LZ99) have found that the presence of the giant planets has an important effect on the structure of the debris disk that is presumably generated in the Kuiper belt (KB): Neptune creates a ringlike structure between 35 and 50 AU, due to the trapping of particles in exterior MMRs, and Jupiter and Saturn are responsible for the ejection of about 80% of particles from the solar system (Liou, Zook, & Dermott 1996, hereafter LZD96). The latter creates a clearing in the inner 10 AU that resembles the inner gap in the β Pic disk. If observed from afar, the KB disk would be the brightest extended feature in the solar system, and its structure, if spatially resolved, could be recognized as harboring at least two giant planets: an inner planet (Jupiter plus Saturn) and an

¹ Steward Observatory, University of Arizona, 933 North Cherry Avenue, Tucson, AZ 85721; amaya@as.arizona.edu.

² Department of Planetary Sciences, University of Arizona, 1629 East University Boulevard, Tucson, AZ 85721.

outer planet (Neptune; LZD96). In anticipation of future observations of debris disks, whose structure is likely to be spatially unresolved, in this paper we are interested in studying how the structure affects the shape of the disk spectral energy distribution (SED) and, consequently, whether the SED can be used to infer the presence of planets.

In this paper, we will follow numerically, from source to sink, the evolution of several hundred dust particles from the KB in the size range from 1 to 40 μm (for $\rho = 2.7 \text{ g cm}^{-3}$), or from 3 to 120 μm (for $\rho = 1 \text{ g cm}^{-3}$), under the combined effects of solar gravity, solar radiation pressure, P-R and solar wind drag, and the gravitational forces of seven planets (excluding Mercury and Pluto). The sinks of dust included in our numerical simulations are (1) ejection into unbound orbits, (2) accretion onto the planets, and (3) orbital decay to less than 0.5 AU heliocentric distance. The equations of motion are integrated using a modification of the multiple time step symplectic method SyMBA (Duncan, Levison, & Lee 1998, hereafter DLL98). In § 2, we describe our numerical integration method and the tests performed to check the suitability of the code. Section 3 describes our methods for deriving the equilibrium spatial distribution of the dust disk. Section 4 explains the distribution of parent bodies and the orbital evolution of dust. In § 5, we discuss the formation of structure in the KB debris disk and its observational signatures. Dust destruction processes are discussed in § 6, and § 7 summarizes our results.

2. NUMERICAL METHOD

In order to study the dynamics of dust from the KB, we need to solve the problem of the dynamical evolution of micron-sized particles, under the effect of gravitational forces of the Sun and the planets and radiation and solar wind forces. This has been solved in the past using the adaptive step size Runge-Kutta integrator RADAU (LZD96; Liou & Zook 1997; Kortenkamp & Dermott 1998; LZ99; Liou, Zook, & Jackson 1999). Another possible choice is the standard mixed-variable symplectic (MVS) integrator, developed by Wisdom & Holman (1991). Its advantage over implicit Runge-Kutta integrators is its speed, about an order of magnitude faster (Wisdom & Holman 1991). This is why the MVS method is now used in long-term studies of the solar system, allowing one to reach integration times approaching the age of the system. Its disadvantage, however, is that it cannot handle close encounters among bodies. Since the outcome of close encounters between the dust particle and the planets is critical for the study of the dynamical evolution of dust grains, previous researchers have chosen RADAU as their numerical integrator. But recently, DLL98 have developed a new multiple time step symplectic algorithm, SyMBA, that can handle close encounters in a symplectic way, thus retaining the speed of the MVS method while being able to overcome its main disadvantage.

The equations of motion of the N -body system are integrated using a variation of SyMBA called SKEEL, which we have modified to include radiation forces. In this section, we summarize the main features of SKEEL as described by DLL98, followed by a description of how radiation forces were introduced and the tests that we have performed to check the validity of our results.

2.1. The Multiple Time Step Symplectic Integrator SKEEL

SKEEL solves the Newtonian gravitational N -body problem by separating its Hamiltonian,

$$H(\mathbf{Q}_i, \mathbf{P}_i) = \sum_{i=1}^n \left(\frac{|\mathbf{P}_i|^2}{2m_i} - \frac{Gm_i m_0}{|\mathbf{Q}_i|} \right) + \frac{|\mathbf{P}_0|^2}{2m_{\text{tot}}} + \frac{1}{2m_0} \left| \sum_{i=1}^n \mathbf{P}_i \right|^2 - \sum_{i=1}^{n-1} \sum_{j=i+1}^n \frac{Gm_i m_j}{|\mathbf{Q}_i - \mathbf{Q}_j|} \quad (1)$$

into three integrable components:

$$H(\mathbf{Q}_i, \mathbf{P}_i) = H_{\text{Kep}} + H_{\text{Sun}} + H_{\text{int}}, \quad (2)$$

where

$$H_{\text{Kep}} = \sum_{i=1}^n \left(\frac{|\mathbf{P}_i|^2}{2m_i} - \frac{Gm_i m_0}{|\mathbf{Q}_i|} \right), \quad (3)$$

$$H_{\text{Sun}} = \frac{1}{2m_0} \left| \sum_{i=1}^n \mathbf{P}_i \right|^2, \quad (4)$$

$$H_{\text{int}} = - \sum_{i=1}^{n-1} \sum_{j=i+1}^n \frac{Gm_i m_j}{|\mathbf{Q}_i - \mathbf{Q}_j|}. \quad (5)$$

\mathbf{Q}_i and \mathbf{P}_i are, respectively, the heliocentric positions and barycentric momenta (if $i \neq 0$) and the position of the center of mass and the total momentum of the system (if $i = 0$); m_{tot} is the total mass of the system. The contribution from the second term in the right-hand side of equation (1) is ignored because it corresponds to the free motion of the center of mass. A second-order symplectic integrator consists in approximating the time evolution by the following symmetrized sequence of steps:

$$E_{\text{Sun}}\left(\frac{\tau}{2}\right) E_{\text{int}}\left(\frac{\tau}{2}\right) E_{\text{Kep}}(\tau) E_{\text{int}}\left(\frac{\tau}{2}\right) E_{\text{Sun}}\left(\frac{\tau}{2}\right), \quad (6)$$

where $E_i(\tau)$ is the evolution under H_i for time τ . For each body there is (1) a linear drift in position by $(\tau/2m_0) \sum \mathbf{P}_i$, to account for the motion of the Sun with respect to the barycenter; (2) a kick to its momentum for time $(\tau/2)$, to account for the gravitational forces of all the massive bodies except the Sun; (3) an evolution along a Kepler orbit for time τ ; (4) another kick like No. 2; and (5) another linear drift like No. 1. During a close encounter between a particle and a planet, the contribution from the encountering planet is separated from the rest so that the time evolution becomes

$$E_{\text{Sun}}\left(\frac{\tau}{2}\right) E_{\text{int}}^{\text{ne}}\left(\frac{\tau}{2}\right) E_{\text{int}}^{\text{enc}}\left(\frac{\tau}{2}\right) E_{\text{Kep}}(\tau) \times E_{\text{int}}^{\text{enc}}\left(\frac{\tau}{2}\right) E_{\text{int}}^{\text{ne}}\left(\frac{\tau}{2}\right) E_{\text{Sun}}\left(\frac{\tau}{2}\right), \quad (7)$$

where $E_{\text{int}}^{\text{ne}}$ refers to the contribution to H_{int} from all the planets except the one in the encounter and $E_{\text{int}}^{\text{enc}}$ is the same, but for the planet in the encounter only. The close-encounter algorithm, represented by

$$E_{\text{int}}^{\text{enc}}\left(\frac{\tau}{2}\right) E_{\text{Kep}}(\tau) E_{\text{int}}^{\text{enc}}\left(\frac{\tau}{2}\right), \quad (8)$$

is as follows: The two-body potential terms in H_{int} , due to

the encountering planet, are decomposed into

$$\frac{Gm_i m_j}{|\mathbf{Q}_i - \mathbf{Q}_j|} = \sum_{k=0}^{\infty} V_k. \quad (9)$$

(For details about the conditions the V_k need to satisfy and the particular functions used in SKEEL, see DLL98.) The multiple time step method consists then in applying equation (8) recursively,

$$\begin{aligned} E_{\Sigma_0}(\tau) &\approx E_0\left(\frac{\tau_0}{2}\right) E_{\Sigma_1}(\tau_0) E_0\left(\frac{\tau_0}{2}\right) \\ &\approx E_0\left(\frac{\tau_0}{2}\right) \left[E_1\left(\frac{\tau_1}{2}\right) E_{\Sigma_2}(\tau_1) E_1\left(\frac{\tau_1}{2}\right) \right]^M E_0\left(\frac{\tau_0}{2}\right), \end{aligned} \quad (10)$$

where $E_i(\tau)$ and $E_{\Sigma_i}(\tau)$ are the evolution for time τ under V_i and $H_{\text{Kep}} + H_{\text{Sun}} + \sum_{k=i}^{\infty} V_k$, respectively. At each level of recursion, the evolution under $E_{\Sigma_i}(\tau)$ is approximated by (1) evolution under V_i for $\tau/2$, (2) M second-order steps of length τ , and (3) evolution under V_i for $\tau/2$. This is equivalent to placing concentric shells around the massive body; the smaller the shell, the smaller the time step associated with it, allowing one to resolve periplanet passage. In particular, DLL98 used $\tau_k/\tau_{k+1} = M$; for our runs, $M = 3$. Note that this multiple time step algorithm only activates during close encounters. When the bodies are farther apart, the algorithm reduces to equation (6); this is because $\{H_{\text{Sun}}, H_{\text{Kep}}\} = \{H_{\text{Sun}}, H_{\text{int}}\} = 0$, so that the pairs are interchangeable.

We use units in which $G = 1$; the unit of mass is $1 M_{\odot}$, the unit of length is 1 AU, and the unit of time is the period of a massless particle at 1 AU divided by 2π .

2.2. Radiation Pressure, Poynting-Robertson Effect, and Solar Wind Drag

A particle of mass μ and geometric cross section A , at heliocentric position \mathbf{r} , moving with velocity \mathbf{v} with respect to a central body of mass m_0 , which is the source of a radiation field of energy flux density $S = L/4\pi r^2$, experiences a force due to the absorption and reemission of radiation that is given (to terms of order v/c) by

$$\frac{d^2\mathbf{r}}{dt^2} = \frac{-Gm_0(1-\beta)}{r^3} \mathbf{r} - \frac{\beta_{\text{sw}} Gm_0}{c} \left[\left(\frac{\dot{\mathbf{r}}}{r} \right) \mathbf{r} + \mathbf{v} \right], \quad (11)$$

where β is a dimensionless constant equal to the ratio between the radiation pressure force, $F_r = SAQ_{\text{pr}}/c$, and the gravitational force, $F_g = Gm_0\mu/r^2$, so that for spherical grains $\beta = F_r/F_g = SAQ_{\text{pr}}r^2/Gm_0\mu c = (3L/16\pi Gm_0c)(Q_{\text{pr}}/\rho s)$. For the Sun, $\beta = 5.7 \times 10^{-5} Q_{\text{pr}}/\rho s$, where ρ and s are the density and radius of the grain in cgs units (Burns et al. 1979). The term Q_{pr} is the radiation pressure coefficient, a measure of the fractional amount of energy scattered and/or absorbed by the grain. The term Q_{pr} is a function of the physical properties of the grain and the wavelength of the incoming radiation; the value we use is an average integrated over the solar spectrum. The advantage of using the dimensionless parameter β is that it is independent of distance, being a function only of the particle size and composition. $\beta_{\text{sw}} = (1 + \text{sw})\beta$, where “sw” is the ratio of the solar wind drag to the P-R drag; in this paper, we use a constant value $\text{sw} = 0.35$ (Gustafson 1994).

The Hamiltonian associated with the first term in the right-hand side of equation (11) is H_{Kep} in equation (3), with $m_0(1-\beta)$ instead of m_0 . Physically, this means that radiation pressure reduces the effective mass of the Sun for the dust grain. In our numerical integrator, called SKEEL-RAD, we introduce the second term in equation (11), the P-R and solar wind drag term, as an additional *kick* to the momentum of the particle. The algorithm thus becomes

$$E_{\text{Sun}}\left(\frac{\tau}{2}\right) E_{\text{int}}^{\text{rad}}\left(\frac{\tau}{2}\right) E_{\text{Kep}}^{\text{rad}}(\tau) E_{\text{int}}^{\text{rad}}\left(\frac{\tau}{2}\right) E_{\text{Sun}}\left(\frac{\tau}{2}\right). \quad (12)$$

In the inertial reference frame, the P-R drag can be thought of as a *mass-loading drag*: the reemitted radiation emits more momentum into the forward direction of motion because of the Doppler effect, which means that the particle loses momentum; since the mass is conserved, the particle is decelerated (there is a drag force). In the particle's reference frame, it originates from the aberration of the radiation, which generates a drag force.

2.3. Comparison with Analytical Results

There is no analytic solution to the general problem of a particle moving under the effect of gravitational forces from the Sun and the planets and radiation and solar wind forces. For this reason, the code cannot be tested in the most general case. But there are analytic solutions for the evolution of the orbital elements of a particle under the effect of radiation in the two-body problem (Wyatt & Whipple 1950; Burns et al. 1979) and in the circular restricted three-body problem (Liou & Zook 1997). We will use these solutions to test the numerical procedure and the validity of our results.

2.3.1. Jacobi Constant Conservation

In the circular restricted three-body problem, consisting of a massless particle, a central mass, and a planet in

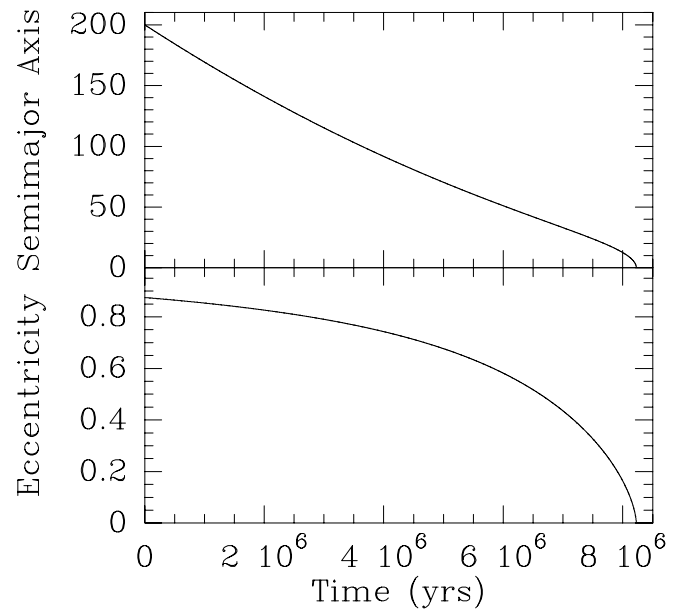


FIG. 1.—Evolution of a and e for a particle with $\beta = 0.2$ and $\text{sw} = 0.35$ in the two-body problem. The solid and the dotted lines coincide and represent the numerical and analytical results, respectively.

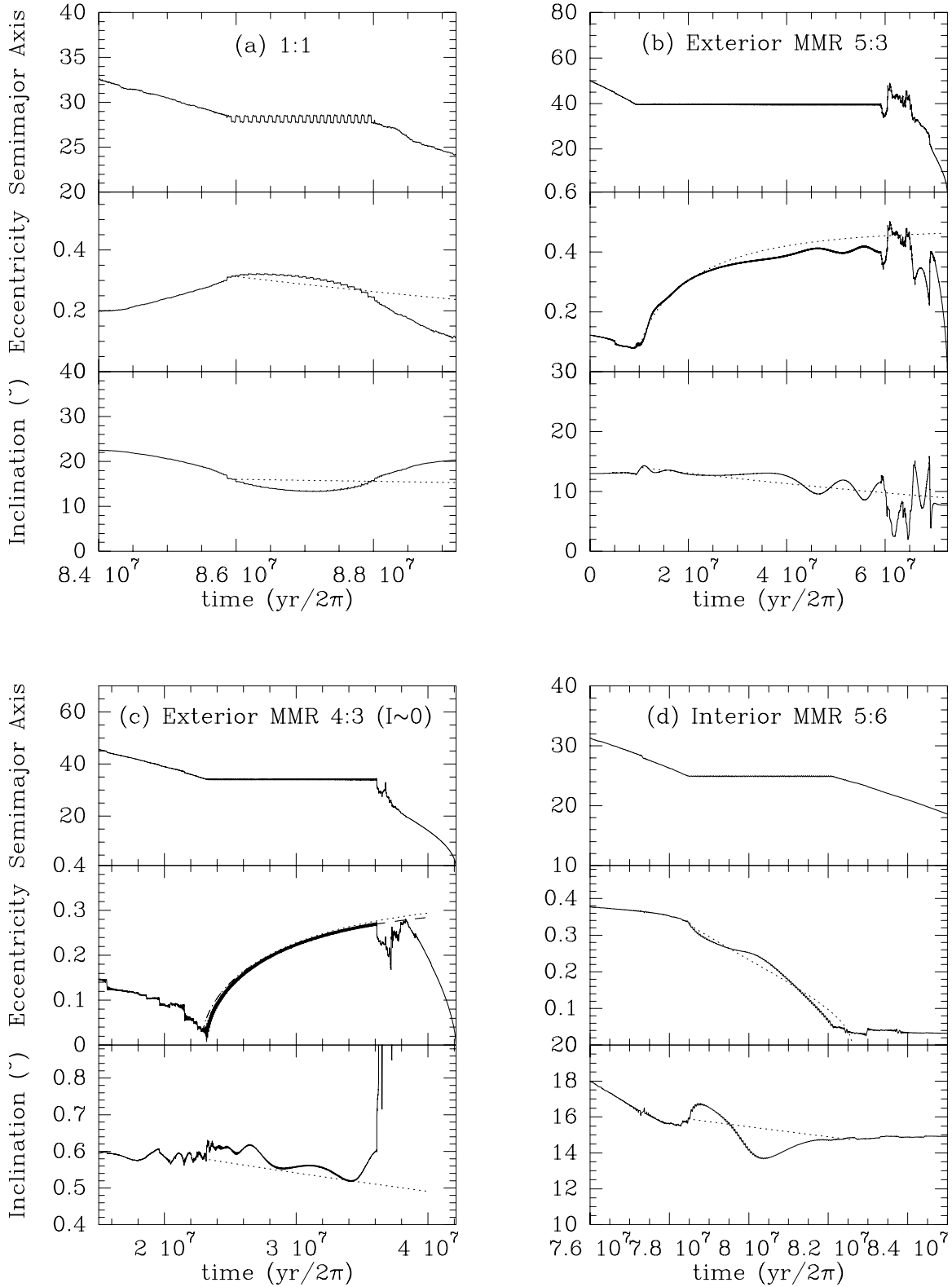


FIG. 2.—Comparison between numerical (*solid line*) and analytical results for the evolution of the orbital elements of $1\ \mu\text{m}$ pyroxene dust particles ($\beta = 0.17$, $\text{sw} = 0.35$) in a circular Sun-Neptune-dust system. Neptune is placed at 30 AU with $e = 0$. The dotted lines represent the analytical results given by eqs. (19) and (20; valid to second order in eccentricity and inclination), and the dashed line corresponds to eq. (18; valid for all eccentricities when $i = 0^\circ$). (a) A particle trapped for 2 Myr in the 1 : 1 MMR with Neptune. Since the eccentricity is already quite large at the time of trapping ($e \sim 0.3$), the agreement with eq. (19) is not very good. (b) A particle trapped for 50 Myr in the exterior 5 : 3 MMR with Neptune. The agreement is very good until the eccentricity reaches ~ 0.3 , at which point it starts to deviate. (c) A particle trapped for 14 Myr in the exterior 4 : 3 MMR with Neptune. At the time of trapping, the inclination is very small ($\sim 0.6^\circ$). The evolution of the eccentricity is perfectly described by eqs. (18) and (19). (d) A particle trapped for 4 Myr in the interior 5 : 6 MMR with Neptune. The overall evolution of eccentricity and inclination are described reasonably well by eq. (19). The semimajor axis stays constant as the eccentricity decreases until it reaches the limiting value of zero, the point at which the particle leaves the resonance.

a circular orbit, the Jacobi constant is an integral of the motion. We have integrated the orbits of 50 massless particles in the presence of the Sun and Neptune (with $a = 30$ AU and $e = 0$). The semimajor axes of the particles were uniformly distributed between 36 and 40 AU and the perihelion distance was set to 30 AU. We use a step size of 2 yr and an integration time of 10^9 yr. We found that 34 out of 50 particles have close encounters, with $\Delta J/J(0) \sim O(10^{-6})$ to $O(10^{-7})$. The remaining 16 that do not suffer close encounters have $\Delta J/J(0) \sim O(10^{-8})$. The worst Jacobi conservation has $\Delta J/J(0) \sim 7 \times 10^{-6}$. These results suggest that close encounters are integrated accurately.

2.3.2. Rates of Change of Orbital Elements

Burns et al. (1979), following Wyatt & Whipple (1950), derived the time rates of change (averaged over an orbit) of semimajor axis (a), eccentricity (e), and inclination (i), of a particle in the two-body problem in the presence of radiation and solar wind forces,

$$\left(\frac{da}{dt}\right)_{\text{P-R}} = -\frac{(1 + \text{sw})\beta m_0}{c} \frac{2 + 3e^2}{a(1 - e^2)^{3/2}}, \quad (13)$$

$$\left(\frac{de}{dt}\right)_{\text{P-R}} = -\frac{5(1 + \text{sw})\beta m_0}{2c} \frac{e}{a^2(1 - e^2)^{1/2}}, \quad (14)$$

$$\left(\frac{di}{dt}\right)_{\text{P-R}} = 0. \quad (15)$$

Figure 1 presents the evolution of a and e for a particle with $\beta = 0.2$ and $\text{sw} = 0.35$. The agreement between the numerical and analytical results is perfect.

When radiation is introduced into the circular restricted three-body problem, the Jacobi constant is no longer an integral of the motion. Using the time variation of the Jacobi constant due to radiation and solar wind forces, together with the time rate of change of the Tisserand criterion, Liou & Zook (1997) have derived analytic expressions that describe the orbital evolution of a particle trapped in an MMR with a planet. The equation relating the time variation in e and i is

$$e(1 - e^2)^{-1/2} \cos i \frac{de}{dt} + (1 - e^2)^{1/2} \sin i \frac{di}{dt} = \frac{(1 + \text{sw})\beta m_0}{a^2 c} \left[\cos i - \frac{a_{\text{pl}}^{3/2}(3e^2 + 2)(1 - \beta)^{1/2}}{2a^{3/2}(1 - e^2)^{3/2}} \right], \quad (16)$$

where a and a_{pl} are the semimajor axes of the resonant orbit and the planet, respectively, related by

$$a = a_{\text{pl}}(1 - \beta)^{1/3}(p/q)^{2/3}. \quad (17)$$

In the particular case when $i = 0$,

$$\dot{e} = \frac{(1 + \text{sw})\beta m_0(1 - e^2)^{1/2}}{a^2 c e} \left[1 - \frac{a_{\text{pl}}^{3/2}(3e^2 + 2)(1 - \beta)^{1/2}}{2a^{3/2}(1 - e^2)^{3/2}} \right]. \quad (18)$$

The expansion of equation (16) to second order in e and i allows one to decouple their time variations; after integrating the resulting two differential equations, Liou & Zook (1997) arrive at these equations (valid only for e -type

resonances):

$$e^2 = \left[e_0^2 - \frac{K - 1}{3} \right] \exp\left(-\frac{3A}{K}t\right) + \frac{K - 1}{3}, \quad (19)$$

$$i = i_0 \exp\left(-\frac{1}{4}At\right), \quad (20)$$

where $A = 2(1 + \text{sw})\beta m_0/a^2 c$ and $K = p/q$; p and q are the two integers that specify the $p : q$ resonance ($K > 1$ for exterior MMRs and $K < 1$ for interior MMRs). To carry out the comparison between analytical and numerical results, we have followed the orbital evolution of 100 pyroxene dust particles, $1 \mu\text{m}$ in diameter ($\beta = 0.17$, $\text{sw} = 0.35$) in a circular Sun-Neptune system. The different panels in Figure 2 show the evolution of four of these particles trapped in the 1 : 1, 5 : 3, 4 : 3, and 5 : 6 MMRs with Neptune ($a = 30$ AU, $e = 0$). The agreement with equation (19) is good for small eccentricities, where the analytical expression holds. We conclude that the code is treating radiation and solar wind forces accurately.

3. EQUILIBRIUM DISTRIBUTION

Ideally, one would like to be able to follow the evolution of a number of particles large enough to resolve the disk structure. However, even though our numerical integrator is very efficient, this task is not feasible with the current computational power. We estimate that for a disk 50 AU in radius, about 10^5 particles would be needed to resolve the structure induced by the solar system planets. To get around this problem, LZ99 used the following approach to obtain the equilibrium spatial distribution of the dust using only 100 particle simulations: First integrate the orbits from their source in the KB until they are either ejected from the solar system or drifted into the Sun, recording the positions of the particles every 1000 yr; then transform the particles' coordinates into a reference frame rotating with the planet dominating the structure (Neptune); and finally accumulate all the rotated coordinates. This yields a time-weighted spatial distribution of the 100 particles over their dynamical lifetime. It is equivalent to the actual spatial density distribution of KB dust provided that (1) the dust production rate is in equilibrium with the loss rate, and (2) the dust particle dynamics is ergodic (i.e., the time-weighting reflects the spatial density). LZ99 point out one limitation of this approach: it assumes the same planetary configuration at the time of release of the dust particles. There are, however, other more important limitations that were overlooked by LZ99. We consider these in detail because this is presently the only feasible approach to the problem of structure formation in debris disks.

3.1. Distribution of Particle Lifetimes

Owing to the ergodic assumption, the debris disk structure obtained using LZ99 approach is determined to a large extent by the longest-lived particles, which represent only a very small fraction of the dust population. The question is, are these particles anomalous, or are they part of a continuous distribution of lifetimes? In the case of anomalies, the structure would be dominated by the dynamics of a very small number of particles of uncertain significance, in which case the structure obtained by the LZ99 approach would not necessarily resemble any equilibrium distribution. If the second option were true, however, the longest-lived

particles would indeed be statistically significant, since they would represent the contribution from an existing population of particles whose lifetimes were part of a long tail in a continuous distribution.

In order to answer this question, we have studied the lifetimes of the particles in all of our models for the solar system

run so far. To facilitate discussion, we include here a list of our models:

Models I-A.—Parent bodies at $a = 45$ AU, $e = 0.1$, and $i = 10^\circ$, four giant planets;

Models I-B.—Same as I-A, but without planets;

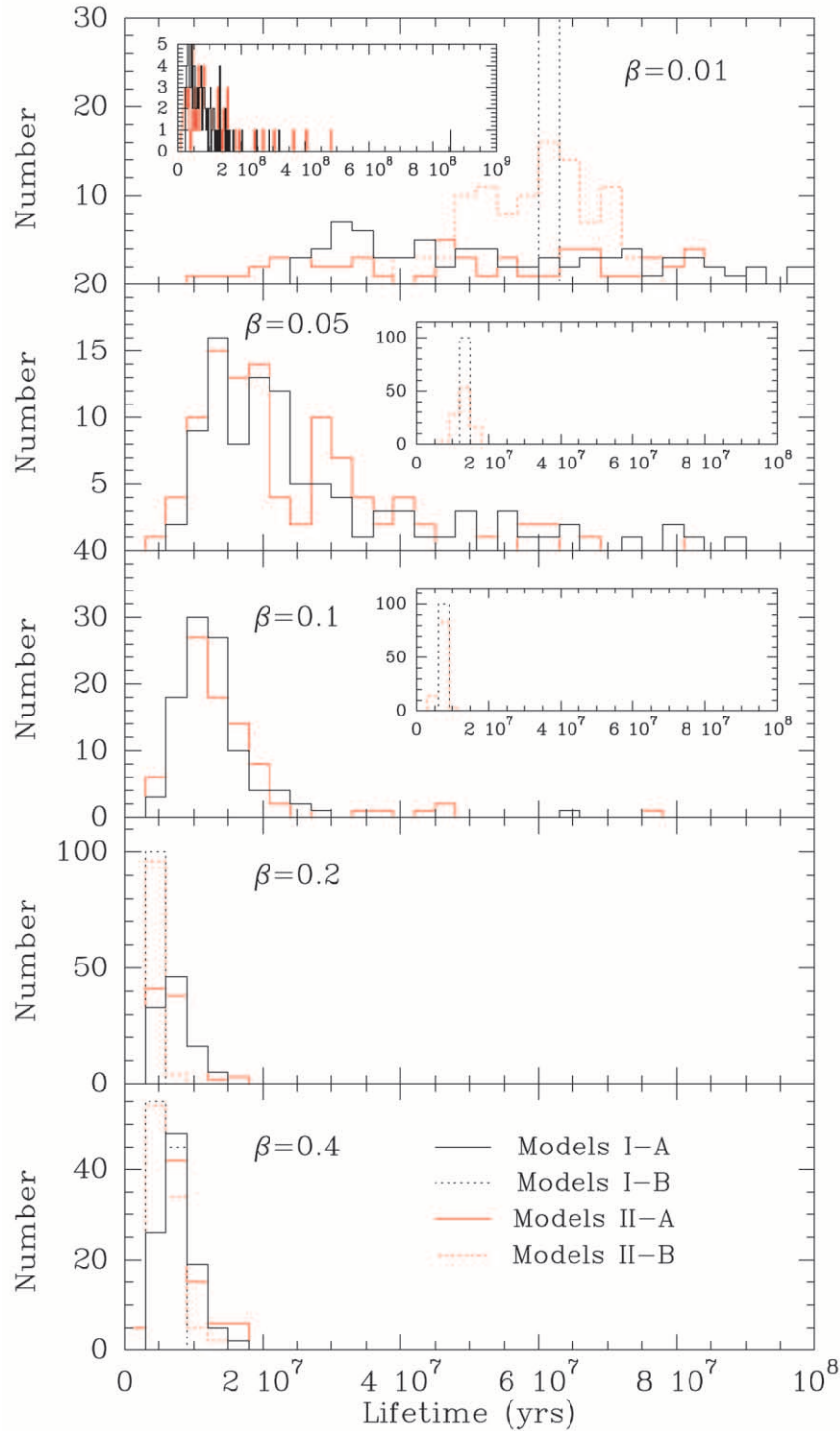


FIG. 3.—Lifetimes of the particles in models I-A (with four planets; black solid line), I-B (without planets; black dotted lines), II-A (with seven planets; red solid line), and II-B (without planets; red dotted lines). The inset for $\beta = 0.01$ is included to show the full time expansion of these very long lived particles. The insets for $\beta = 0.05$ and $\beta = 0.1$ show the no-planet models separately to avoid confusion. The presence of the planets increases the lifetime of the particles. The smaller the β , the larger the difference between the planet and no-planets cases: the trapping into MMRs is more efficient when the drag force is small.

Models II-A.—Parent bodies randomly distributed in the ranges $a = 35\text{--}50$ AU, $q = 35\text{--}50$ AU, and $i = 0^\circ\text{--}17^\circ$, seven planets (excluding Mercury and Pluto);

Models II-B.—Same as II-A, but without planets.

For all models, the mean anomaly (M), longitude of the ascending node (Ω), and argument of perihelion (ω) of dust particles were randomly distributed between 0 and 2π . All models were run with 100 particles each for five different values of β : 0.01, 0.05, 0.1, 0.2, and 0.4. For a density of 2.7 g cm^{-3} , these values correspond to particle sizes of 40, 9, 4, 2, and $1\text{ }\mu\text{m}$, respectively; for 1 g cm^{-3} , they correspond to 120, 23, 11, 6, and $3\text{ }\mu\text{m}$, respectively.

Figure 3 shows the lifetimes for all the particles in our models. For the present discussion, the difference between having four or seven planets is not important. What is important for this argument is that the initial conditions of the parent bodies are different upon release of the dust particles. We see in Figure 3 that the median lifetime and the dispersion of lifetimes are both systematically smaller for larger β . The longer lifetimes are due to longer trapping at exterior MMRs with Neptune. The residence time in an MMR is variable and unpredictable owing to the underlying chaotic resonance dynamics (see Malhotra, Duncan, & Levison 2000). From the point of view of using these simulations to obtain the equilibrium spatial distribution of dust, the most worrisome feature is that the lifetime of the longest-lived particle may be several times longer than the next longest-lived, and more than an order of magnitude greater than the median lifetime. This may be due to numerical errors that affect the behavior of a few particles, or it may be due to the

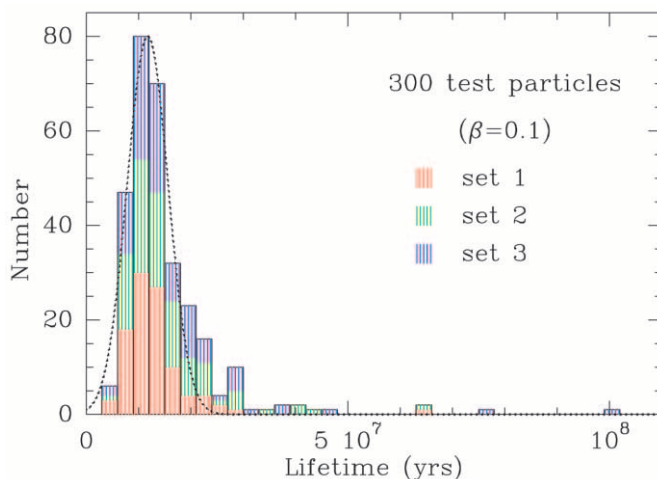


FIG. 4.—Lifetimes for the three models I-A, 100 particles each, plotted together with the different colors representing the contribution from the three different runs. The distribution of lifetimes reassembles that of a Gaussian (dotted line) plus a long tail.

underlying chaotic dynamics that produces a long tail in a continuous distribution of dynamical lifetimes.

To distinguish between these two possibilities, two additional runs of 100 particles each (with different random values of M , Ω , and ω) were done for model I-A with $\beta = 0.1$. The results are shown in Figure 4. We see that with an increasing number of particles, the gap between the longest and next longest lived particle is reduced. Overall, the distribution of lifetimes resembles the sum of a Gaussian and a

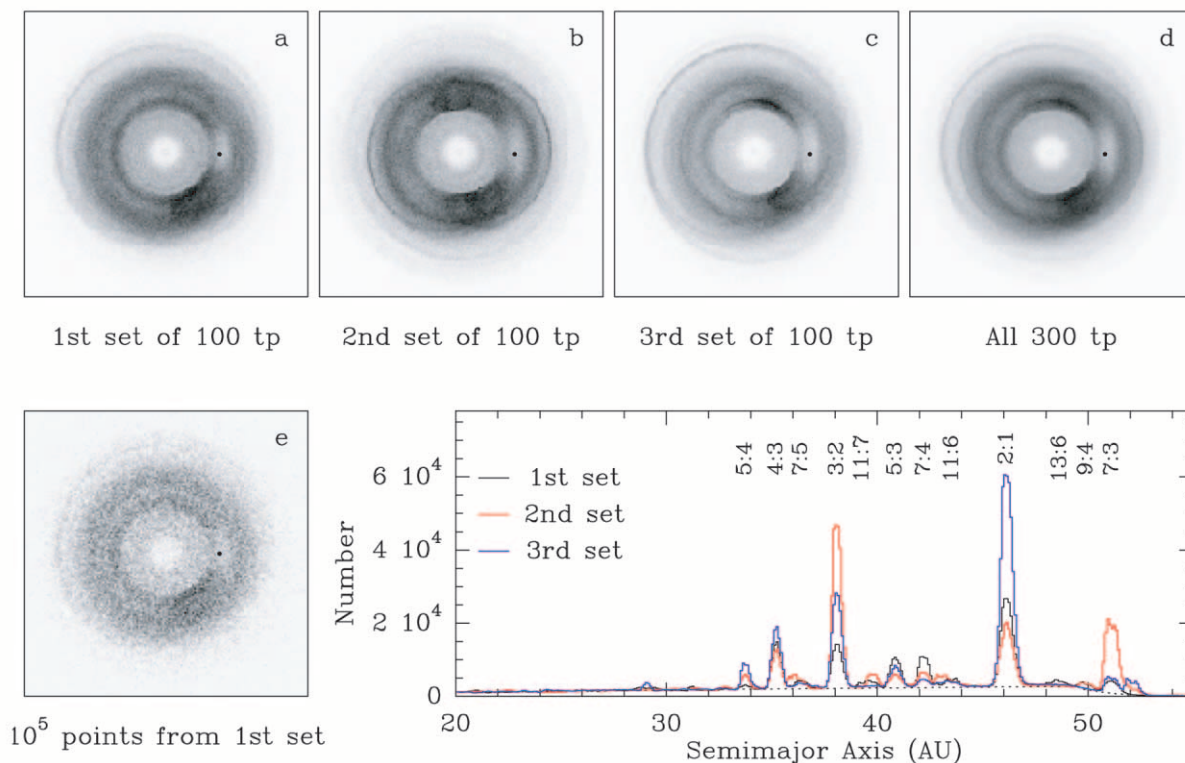


FIG. 5.—(a–c) “Equilibrium” number density distributions for the three models I-A with $\beta = 0.1$. (d) Number density distributions for the 300 particles together. (e) 10^5 randomly selected points from (a), indicating that a large number of particles are needed to resolve the structure. The dot indicates the position of Neptune. The histogram shows the relative occurrence of the different MMRs. The positions of a few MMRs with Neptune are indicated.

uniform distribution. With only a few hundred particles in numerical simulations, we are limited to small numbers of long-lived particles. However, we conclude with some confidence that the longest-lived particles are not anomalous but statistically representative of a real dynamical population.

3.2. Spatial Distribution

Figure 5 shows the “equilibrium” number density distributions that result after applying the LZ99 approach to the three models I-A with $\beta = 0.1$. The relative occurrence of the different MMRs can also be seen in the histogram presented in this figure. Note that the only difference between the three runs is in the initial M , Ω , and ω . We see that the dust particles’ times of residence in various mean resonances with Neptune are highly variable.

Figure 6 shows the radial profiles (averaged over all θ) and angular profiles (integrated between 25 and 35 AU) of the number and brightness (see § 5) density distribution derived from four different sets of 100 particles each. This figure indicates that (1) the LZ99 approach is able to reliably predict the radial structure and (2) the azimuthal structure

is not predictable in detail, except for a “gap” near the outermost planet, Neptune.

We have explored how fast structure is created and the effect of excluding the contribution to the structure from the longest-lived particles. Our results, which are summarized in Figure 7, show that the structure is created quickly and that the radial profiles of the number density distribution do not strongly depend on the contribution from the longest-lived particles. This provides further validation of the LZ99 approach.

4. DISTRIBUTION OF PARENT BODIES AND ORBITAL EVOLUTION OF DUST PARTICLES

KBOs are icy bodies that lie in a disk beyond Neptune’s orbit. It is estimated that there are about 3.5×10^4 objects with diameters greater than 100 km (Jewitt & Luu 1995) in the 30–50 AU annulus. The outer limit of the belt is presently not well determined. Dust production occurs as a result of mutual collisions of KBOs (Backman & Paresce 1993; Backman et al. 1995; Stern 1996) and of collisions with interstellar grains (Yamamoto & Mukai 1998).

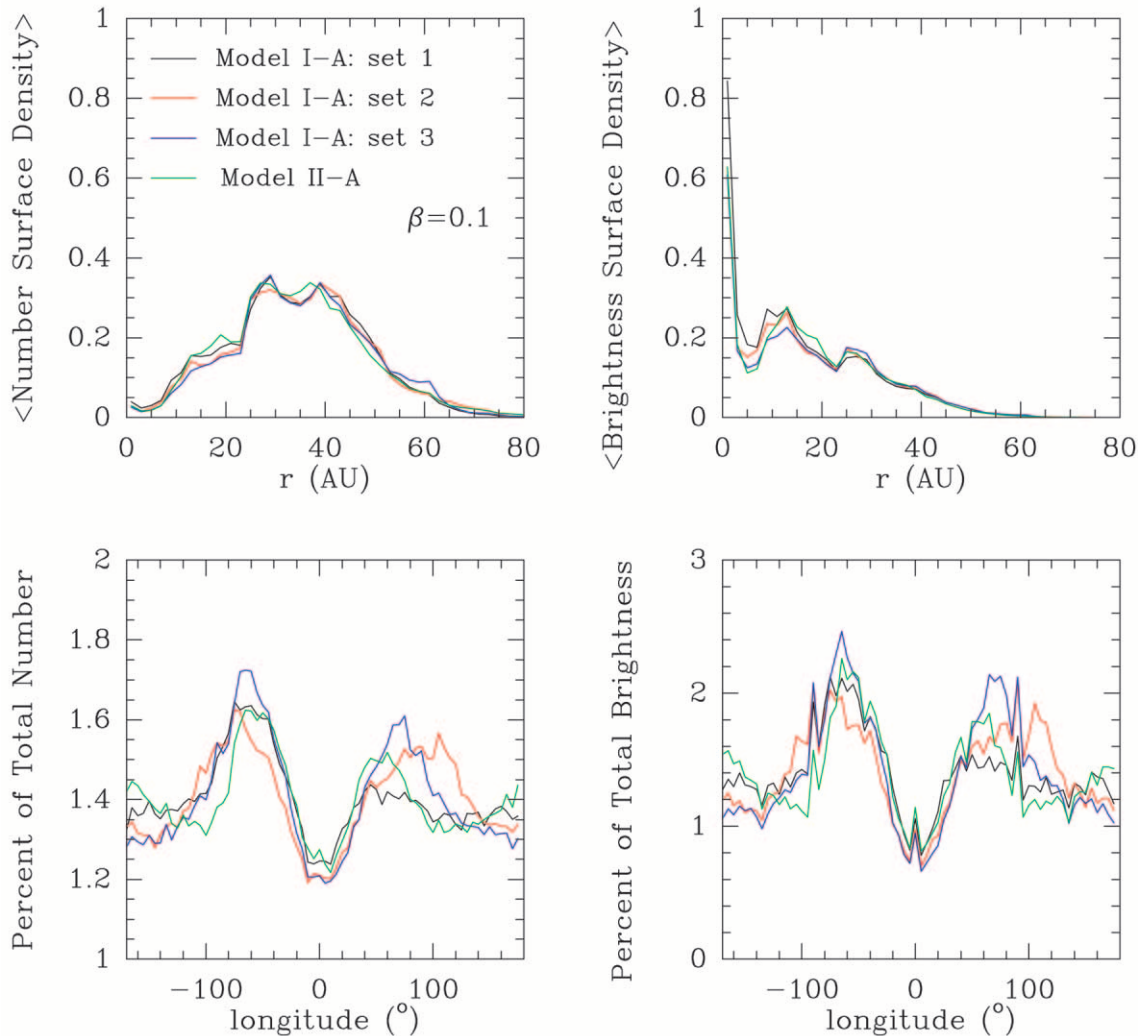


FIG. 6.—*Top*: Number and brightness density radial distributions, averaged over all θ , for particles with $\beta = 0.1$. Black, red, and blue lines correspond to the three models I-A. Green corresponds to the model II-A. *Bottom*: Same as above, but for angular distributions, integrated between 25 and 35 AU. The longitude is measured with respect to Neptune. The LZ99 approach is able to predict the radial structure, but the uncertainties in the azimuthal structure are large.

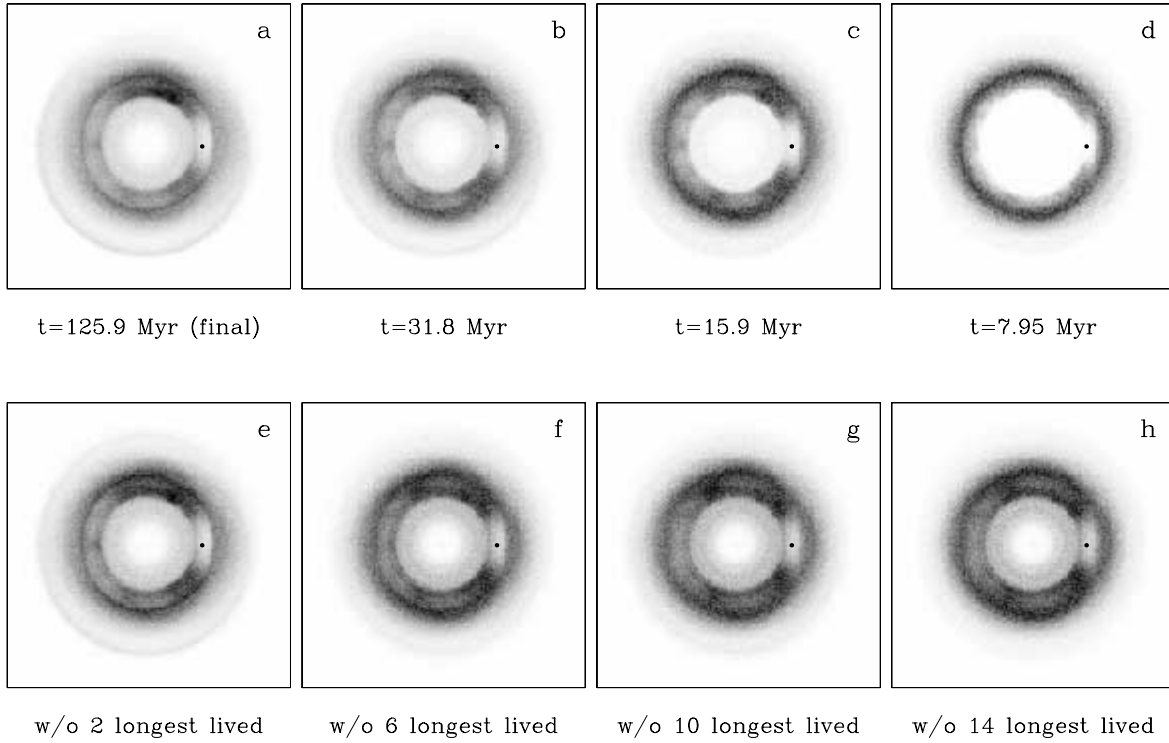


FIG. 7.—*Top*: Timescale in which structure is created. (a) Number density distribution for one of the models I-A with $\beta = 0.1$ by the time the last particle leaves the system (125.9 Myr). (b–d) Structure seen at earlier and earlier times, 31.8, 15.9, and 7.95 Myr, respectively. *Bottom*: Effect of excluding the longest-lived particles. (e–h) Structure after excluding the contribution from the 2, 6, 10, and 14 longest-lived particles, respectively. These results validate the use of the LZ99 approach by indicating that the structure is created quickly and that the radial profiles of the number density distribution do not strongly depend on the contribution from the longest-lived particles. The dot indicates the position of Neptune.

Our selection of the orbital elements of the parent bodies is based on published observations of KBOs and on recent studies of their debiased radial (Trujillo & Brown 2001) and inclination (Brown 2001) distributions. Semimajor axes were uniformly distributed between 35 and 50 AU; eccentricities were derived from perihelion distances, with random values between 35 and 50 AU; inclinations were uniformly distributed between 0° and 17° ; and the other three orbital elements, mean anomaly (M), longitude of ascending node (Ω), and argument of perihelion (ω), were randomly selected between 0 and 2π .

When dust particles are released from their parent bodies ($\beta = 0$), their orbital elements instantaneously change because of the effect of radiation pressure, which, as we saw in § 2.2, makes the particle experience the force of a less massive Sun by a factor of $1 - \beta$. The new semimajor axis (a') and eccentricity (e') in terms of their parent bodies (a and e) are given by

$$a' = a \frac{1 - \beta}{1 - 2a\beta/r}, \quad (21)$$

$$e' = \left| 1 - \frac{(1 - 2a\beta/r)(1 - e^2)}{1 - \beta^2} \right|^{1/2}. \quad (22)$$

Figure 8 shows e and i for the parent bodies and the dust particles at the time of release.

In their slow journey toward the Sun, the particles cross MMRs with the giant planets. As a result, some particles get trapped, and structure in the debris disk begins to form. As reported by LZ99, and also seen in our models, the exterior

resonances with Neptune dominate the trapping. Usually, the particles escape the resonances via close encounters with the planet, but in the case of interior resonances, they can also escape as a result of the decrease of a , which makes the particle move farther away from the planet, where drag forces dominate (Liou & Zook 1997).

We have used the three models I-A with $\beta = 0.1$ to study the existence of correlations in the initial orbital elements of the longest-lived particles. Figure 9 shows a , e , $\lambda - \lambda_{\text{Nep}}$, and M for the 65 longest-lived particles (*solid lines*; these particles have lifetimes $\geq 2 \times 10^7$ yr [see Fig. 4]) compared with all 300 particles in the models (*dotted lines*). There are two prominent features, both readily understood: (1) As the particles are released, and because of their increased semimajor axes, their mean anomaly is such that they avoid aphelion, explaining the gap between 90° and 270° . (2) The longest-lived particles tend to have smaller initial eccentricities, as expected from the fact that they tend to be trapped more easily in resonances. We find no evidence of correlation between lifetime and initial orbital parameters.

5. STRUCTURE FORMATION: THE GIANT PLANETS RESHAPE THE DEBRIS DISK

Figure 10 shows the equilibrium semimajor-axis distributions, Figures 11 and 12 show the equilibrium number density distributions in the presence and absence of planets, and Figure 13 shows the radial profiles averaged over all θ . The main features seen in these figures are (1) the ringlike structure along Neptune's orbit, showing some azimuthal

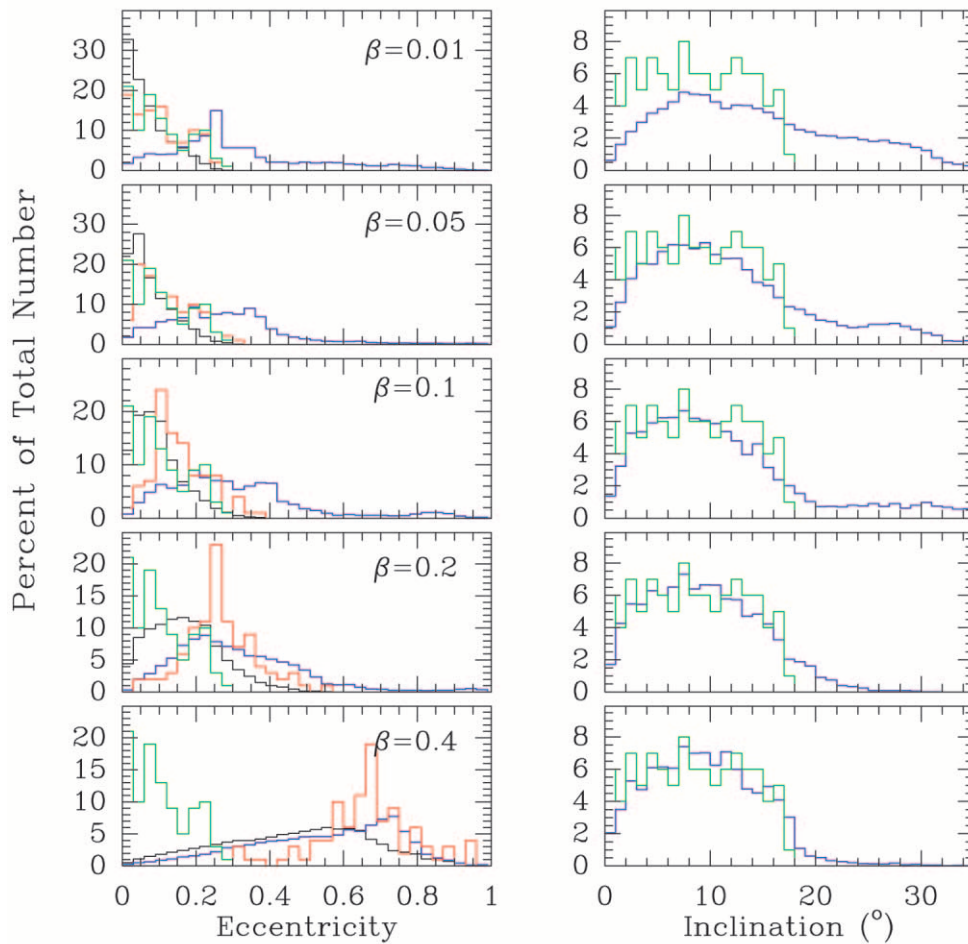


FIG. 8.—Distribution of eccentricities and inclinations for parent bodies (*green*), dust particles at the time of release (*red*), evolved dust particles in models II-A (*blue*), and evolved dust particles in models II-B (*black*). The difference between the presence and nonpresence of planets is more dramatic for smaller values of β . When planets are present, a fraction of the particles have their eccentricities and inclinations increased (because of trapping in e -type and i -type exterior resonances, respectively). Radiation forces do not affect inclination, so the green, red, and black lines coincide.

variation due to MMRs; (2) the minimum density at Neptune's position, as particles in MMRs tend to avoid the perturbing planet; (3) the clearing of dust from the inner 10 AU; and (4) the fact that the structure is more prominent for larger particles (smaller β -values). The latter is because the trapping in MMRs is more efficient when the drag forces are small (LZ99). On the other hand, the ejection of particles from the inner 10 AU does not depend on size. The difference between models I-A and II-A in Figure 10 gives an estimate of the uncertainties, since the effect of the three terrestrial planets is negligible and the only difference is in the initial conditions of the parent bodies. The relative “strength” of the dominant MMRs depends quite strongly on the initial conditions (see also the histogram in Fig. 5). This may indicate that the exact prediction of a planet's orbit, based on the identification of resonances, may be difficult. The ringlike structure in the number density is also visible in the brightness distributions of Figure 11, which were calculated assuming graybody absorption and emission by the dust grains in a $3 \times 10^{-11} M_{\odot}$ single-size grain disk, at a distance of 30 pc. Additional features seen in the brightness distribution are (1) a bright ring between 10 and 15 AU with a sharp inner edge, due to the ejection of particles by Saturn and Jupiter; and (2) a steep increase in brightness in the inner 5 AU. Both features are due to the combination of the

decreasing particle density and increasing grain temperature closer to the Sun.

From the observational point of view, current infrared detector technology does not allow us to spatially resolve many of these features. As an example, the *SIRTF* MIPS 24 μm detector has a pixel size of $2''.45$, which at the distance of β Pic (16.4 pc) means a spatial resolution of 40 AU. For *SIRTF* IRAC (3.6–8.0 μm), the resolution would be about 20 AU. The question is then how much information can be derived from the disk SED. Figure 14 shows the composite SEDs that result from combining the SEDs from the $\beta = 0.01, 0.05, 0.1, 0.2$, and 0.4 disks, with weights in such a way that they follow the power-law distribution $n(a) da = n_0 a^{-3.5} da$, where a is the particle radius. The black lines correspond to the SEDs from a $3 \times 10^{-11} M_{\odot}$ disk. Blue, red, and green lines correspond to the SEDs from a system of the Sun plus a disk with three different masses. In all cases, the solid line is for a system with seven planets, and the dotted line is for a system without planets. The wavelength labels correspond to the *SIRTF* MIPS and IRAC bands potentially useful to study these systems. We see that the presence of planets does modify the disk SED. The main modification is due to the clearing of dust in the inner region (an “inner gap”) by Jupiter and Saturn, which causes a significant deficit in the disk SED at higher frequencies. The

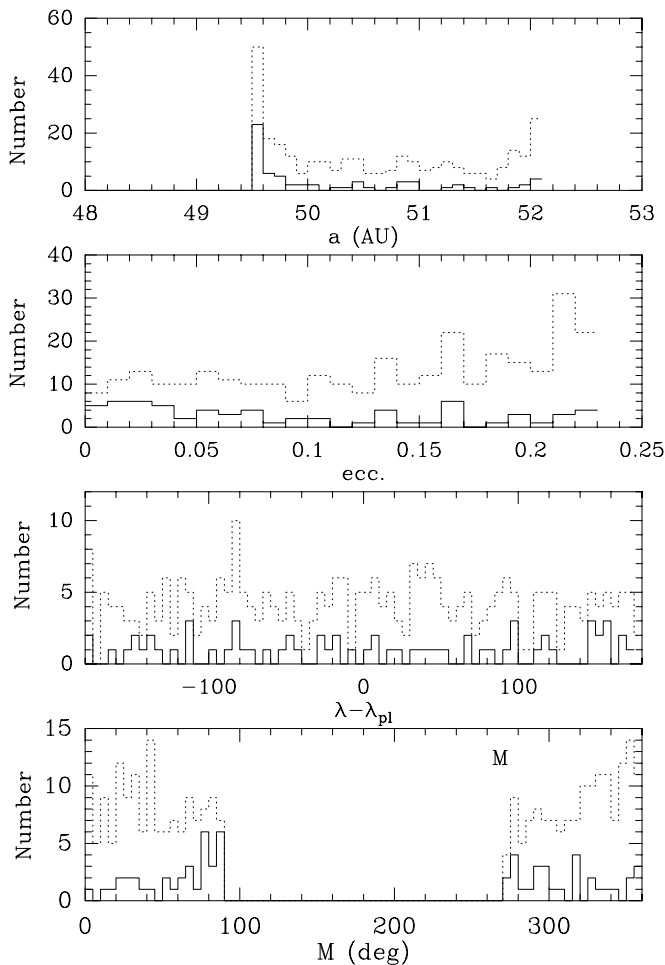


FIG. 9.—Initial orbital elements of the 65 longest-lived particles from the three models I-A with $\beta = 0.1$ (solid line), compared with the total of 300 particles (dotted line). The longest-lived particles tend to have lower e . The gap between 90° and 270° is explained because upon release, due to the increased a , the particles avoid aphelion.

density enhancement in the annulus between 35 and 50 AU, due to trapping in Neptune's exterior MMRs, causes a relatively smaller effect on the shape of the disk SED. How well can one determine the masses and orbits of planetary perturbors from the shape of the disk SED? We plan to address this question in the future by exploring in detail the parameter space of planetary masses and orbital elements.

It is important to note that our model systems (with and without planets) contain the same amount of disk mass. We are interested in how the structure created by the planets affects the shape of the SED, independent of the dust production rate. The latter determines only the normalization factor. However, planetary perturbations can affect the dust production rate, possibly leading to more massive dust disks. This effect is not taken into account in our models but will be considered in the future.

6. DUST-DESTROYING PROCESSES

6.1. Collisions

Particles that, from the dynamical point of view, are able to drift all the way into the Sun may be destroyed by mutual collisions or collisions with interstellar dust grains before

they reach the inner solar system. Based on *Ulysses* measurements of interstellar dust flux at 5 AU, and assuming that this flux is constant throughout the solar system and does not vary in time, the average time for one collision to occur between a spherical grain of diameter d and an interstellar grain of diameter d_i is $t_c = 504/(d + d_i)^2$ Myr (LZD96). Assuming that interstellar dust have an average size of $1.2 \mu\text{m}$, the collisional times for 1, 2, 4, and $9 \mu\text{m}$ particles are 104, 49, 19, and 4.8 Myr, respectively. For densities of 2.7 g cm^{-3} , these sizes correspond to β -values of 0.4, 0.2, 0.1, and 0.05, respectively. KB dust, however, is more likely to have lower densities. Analysis of collected interplanetary dust particles (IDPs) indicate that high-velocity IDPs have fluffy, porous textures with an average density of about 1 g cm^{-3} (Joswiak et al. 2000). For those densities, the sizes corresponding to the β -values above are 3, 6, 11, and $23 \mu\text{m}$. These particles will have collisional times of 28.6, 9.7, 3.4, and 0.86 Myr, respectively. In these size ranges mutual collisions are not as important as collisions with interstellar grains (LZD96). If so, comparing the collisional times and the dynamical lifetimes in Figure 3 shows that collisional destruction is only important for grains larger than about $6 \mu\text{m}$. Smaller particles will therefore survive collisions and drift all the way into the Sun, contributing to the zodiacal cloud. Particles larger than $50 \mu\text{m}$ may also survive collisions because interstellar grains are too small to destroy these in a single impact, so it is possible that they are able to evolve into the inner solar system (LZD96). Figure 7 shows the timescale for disk structure formation in the case of $\beta = 0.1$. Structure is already beginning to form by about 8 Myr; by 16 Myr, the structure shows almost all the features of the equilibrium state. Collisional timescales for $\beta = 0.1$ range from 3.4 to 19 Myr, depending on the density. It is therefore not clear that disk structure for these particles sizes is able to survive collisions. For smaller particles (larger β) structure will survive, but these particles do not have as prominent a structure associated with the exterior MMRs with outer planets (see Fig. 5). Although all these results should be taken with caution, since the flux and the size distribution of the interstellar grains are rather uncertain, what is clear is that one should keep in mind collisions with interstellar grains when trying to infer the presence of planets from the study of structure in debris disk (see also LZ99).

6.2. Sublimation

Depending on the composition of dust particles, sublimation may or may not play an important role in dust destruction processes and, therefore, in the ability of dust to reach the inner solar system. For silicates, the sublimation temperature is $\sim 1500 \text{ K}$. For the particles sizes considered in this paper, 1, 2, 4, 9, and $40 \mu\text{m}$ (which correspond to β -values of 0.4, 0.2, 0.1, 0.05, and 0.01 with $\rho = 2.7 \text{ g cm}^{-3}$), this temperature is reached at $r < 0.5 \text{ AU}$, which is the minimum heliocentric distance allowed by our models. In this case, sublimation does not affect the evolution of dust particles and the radial disk structure. But if the KB dust composition is more similar to water ice, the sublimation temperature is $\sim 100 \text{ K}$, which for the sizes of 3, 6, 11, 23, and $120 \mu\text{m}$ (corresponding to the β values above with $\rho = 1 \text{ g cm}^{-3}$) is reached at 27, 19, 14, 10, and 4.3 AU, respectively. In this case, the ability of dust to reach the inner solar system would be greatly diminished by sublimation, even

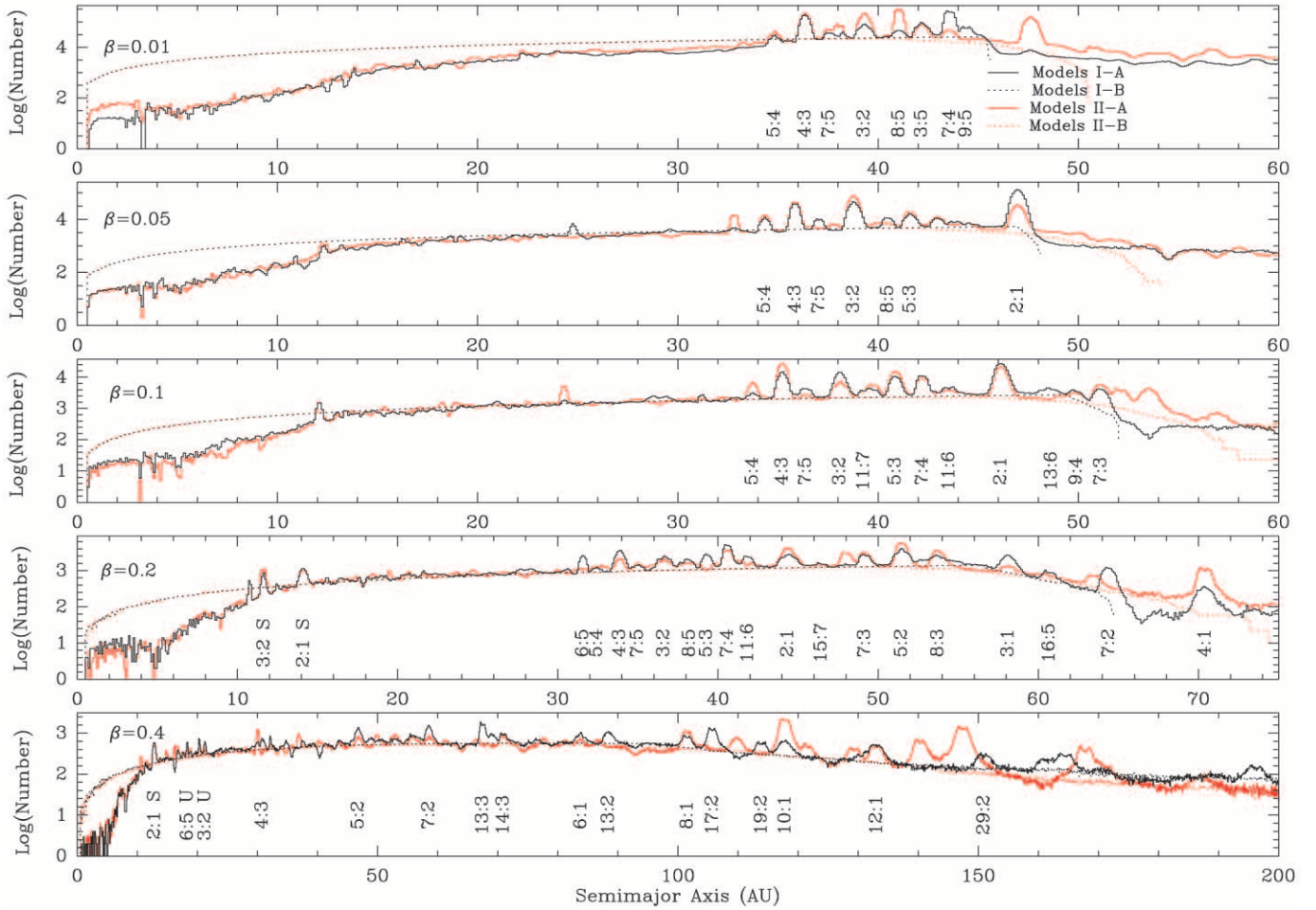


FIG. 10.—“Equilibrium” semimajor-axis distribution in logarithmic scale for the particles in the models I-A (black solid lines), I-B (black dotted lines), II-A (red solid lines), and II-B (red dotted lines). The trapping of particles in the exterior MMRs with Neptune and the depletion of particles in the inner 10 AU in the presence of planets are the most prominent features in the figure.

for dust grains as large as $120 \mu\text{m}$, and the disk structure created by the inner planets would be destroyed.

7. CONCLUSIONS AND FUTURE WORK

1. We have followed, from source to sink, the orbital evolution of dust particles from the Kuiper belt. To integrate the equations of motion efficiently, we have introduced radiation and solar wind forces in the multiple time step symplectic integrator of DLL98. We have established the suitability of our code by comparison between numerical results and analytical solutions with two-body and restricted three-body cases, as well as comparison with other numerical results in the literature (LZD96; LZ99).

2. We have carried out numerical simulations for single-size particle disks in the presence and in the absence of planets in order to estimate the uncertainties inherent in the prediction of structure in the outer solar system debris disk, owing to the chaotic dynamics of dust orbital evolution. We simulate dust particle initial conditions according to the wider distribution of parent bodies indicated by the recent observed distribution of KBOs, and our simulations extend to larger particle sizes than previous studies.

3. We find that the distribution of KB dust particle lifetimes in the solar system are described as the sum of a Gaussian and a nearly uniform distribution; the latter represents only a small fraction of all particles but extends to very long lifetimes, while the Gaussian represents the dominant fraction of particles. The mean and dispersion of the Gaussian component increases systematically with particle size and is in the range of a few million years for $1\text{--}100 \mu\text{m}$ particle sizes. We do not find any correlations between the initial orbital elements and dynamical lifetimes of dust particles.

4. We have examined carefully the method used by LZ99 to estimate the equilibrium spatial distribution of KB dust in the solar system. This method is based on the ergodic assumption, so the dust structures obtained are determined to a large extent by the longest-lived particles, which represent only a very small fraction of the dust population. The ergodic assumption is generally not applicable in chaotic dynamical systems. Nevertheless, we have established that in practice this method gives reliable results for several aspects of dust dynamical studies for three reasons: (a) the distribution of dust particle lifetimes is described as the sum of a Gaussian plus a nearly uniform distribution, that is, the longest-lived particles are not anomalous, they are statistically representative of the long tail population; (b) the dust spatial structure is created quickly; (c) the radial profile of

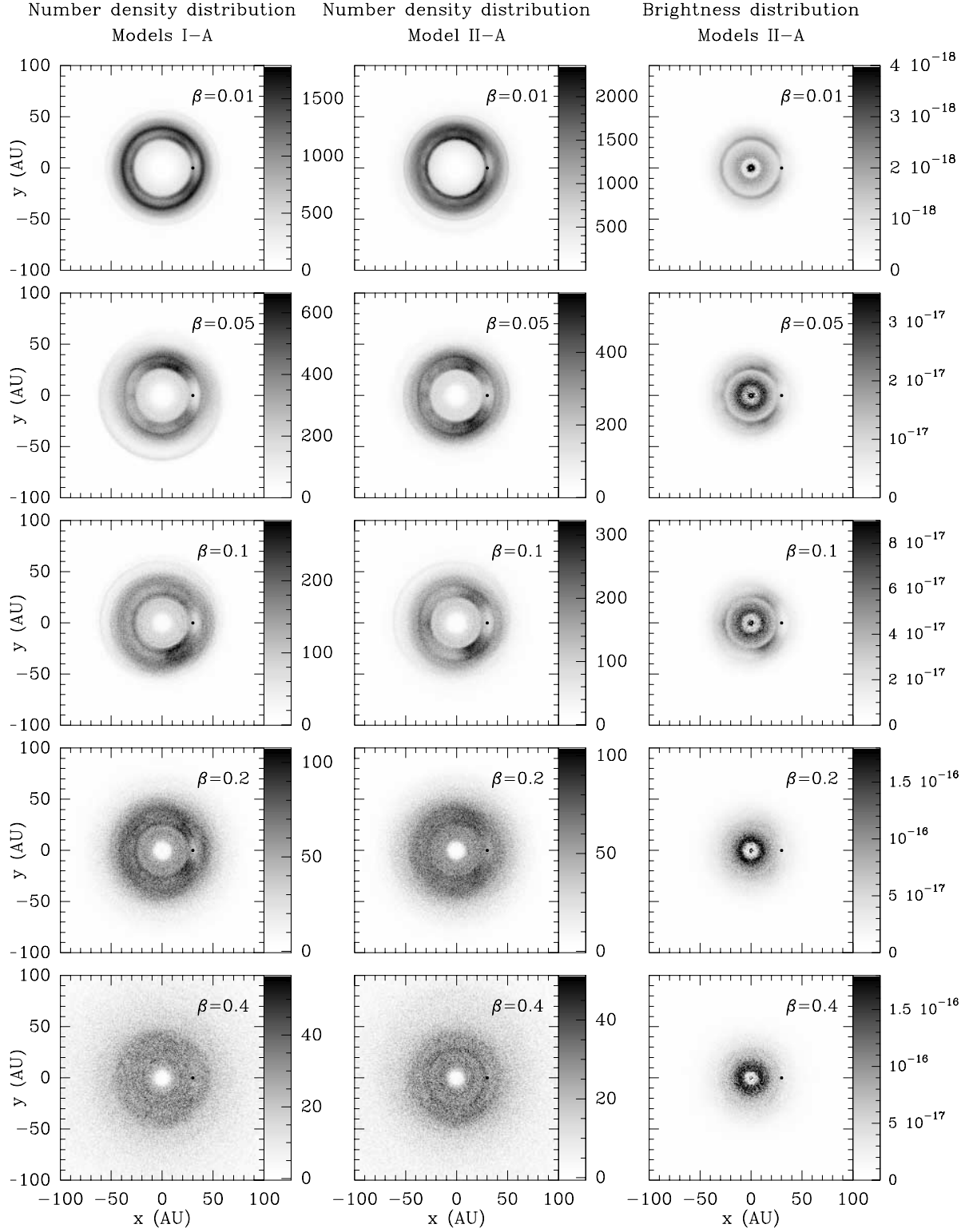


FIG. 11.—“Equilibrium” number density distribution for models I-A and II-A (left and middle columns) and brightness density distribution for model II-A (right column). The brightness density is in units of $\text{ergs s}^{-1} \text{cm}^{-2} (1 \text{ AU})^{-2}$ and corresponds to the thermal emission, integrated from 21.6 to 26.3 μm , of a $3 \times 10^{-11} M_{\odot}$ disk at a distance of 30 pc surrounding a $1 L_{\odot}$ star. Grain temperatures were calculated using the expressions from Backman & Paresce (1993) for the thermal equilibria and emitted spectra of generic grains. Absorptive efficiency was assumed to be $\epsilon = 1$, and emissive efficiency was $\epsilon = 1$ for $\lambda < a$ and $\epsilon = a/\lambda$ for $\lambda > a$, where a is the grain radius. The dust particles have $\rho = 2.7 \text{ g cm}^{-3}$. The dot at (30, 0) indicates the position of Neptune.

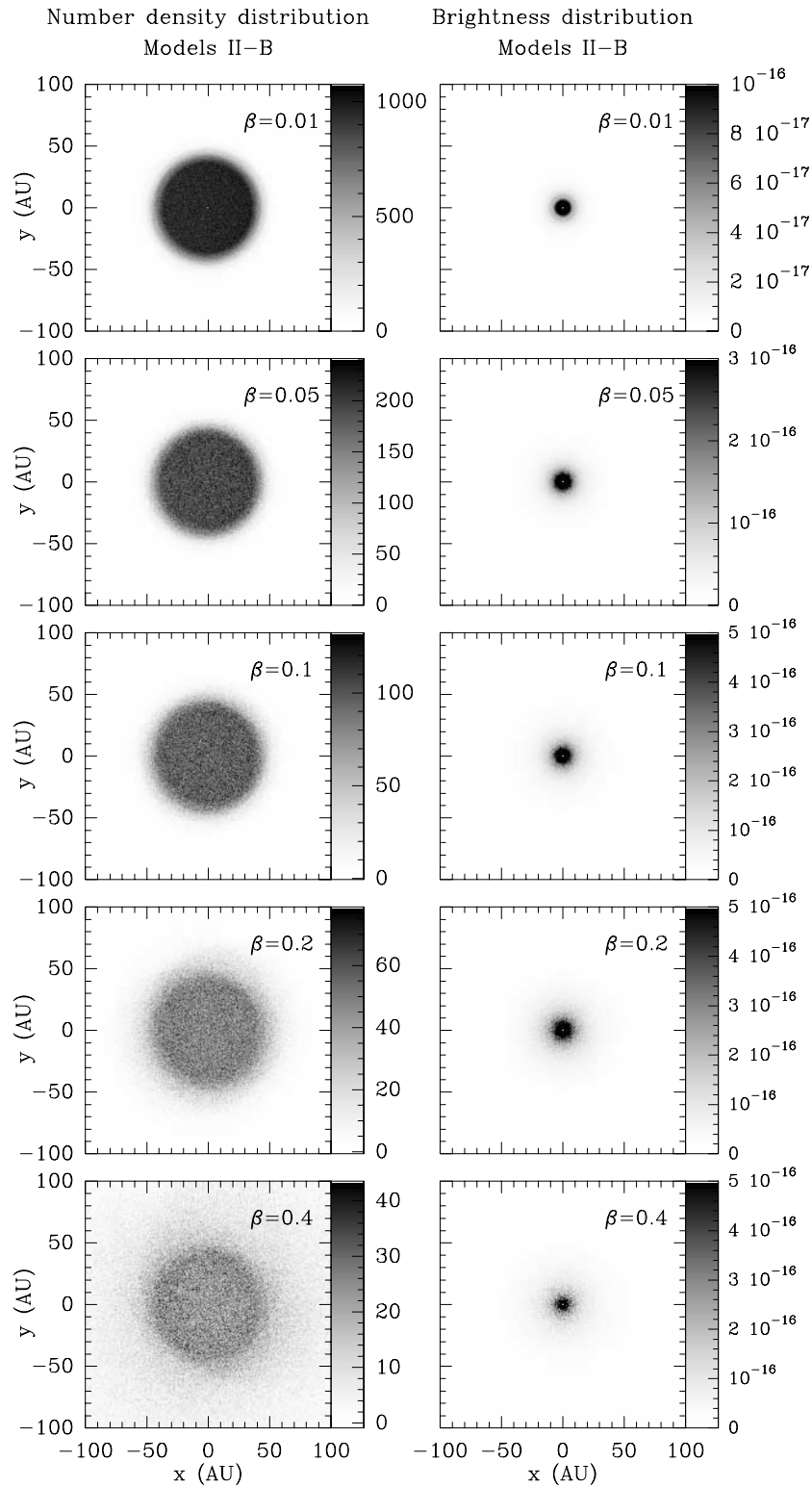


FIG. 12.—Same as Fig. 11, but for the “equilibrium” number and brightness density distributions of models II-B

the equilibrium number density distribution does not strongly depend on the longest-lived particles (although the azimuthal structure does).

5. Overall, the number density of the KB dust disk shows a depletion of dust in the inner 10 AU, due to gravitational scattering by Jupiter and Saturn, and an enhanced dust density in a ring between 35 and 50 AU, due to trapping of

particles in mean motion resonances with Neptune. The structure is more pronounced for larger particle sizes. The brightness distribution shows a bright ring between 10 and 15 AU with a sharp inner edge (particles ejected by Saturn and Jupiter), and a steep increase in brightness in the inner few AU (a combination of the decreasing density and increasing grain temperature).

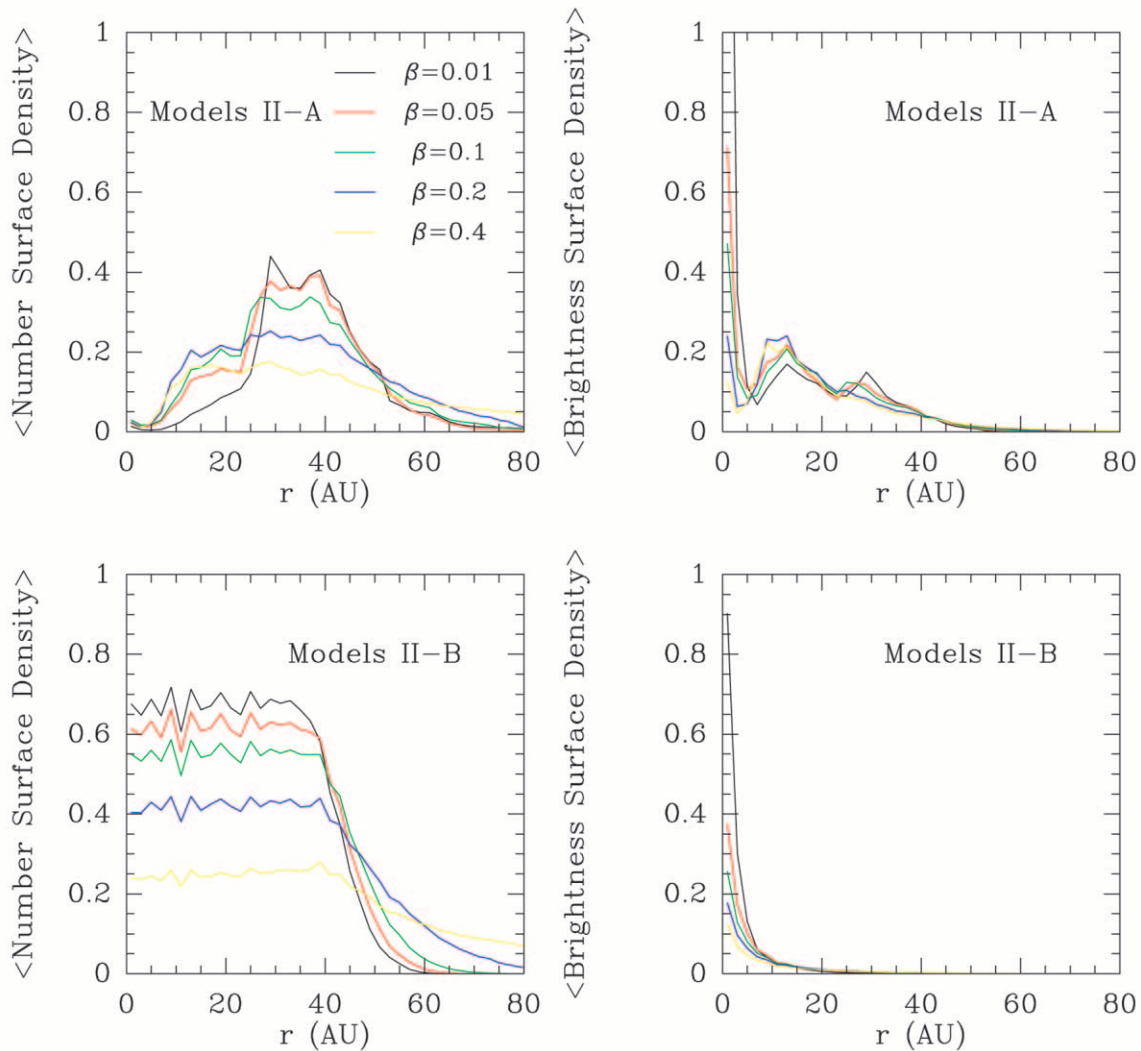


FIG. 13.—Number and brightness surface density radial distributions, averaged over all θ , for models II-A (top) and II-B (bottom) shown in Figs. 11 and 12. The main features are the depletion of particles in the inner 10 AU, due to scattering by Jupiter and Neptune, and the enhancement of particles from 30 to 50 AU, due to trapping in MMRs with Neptune.

6. We find that the azimuthal structure of the dust disk is not predictable in detail, except for a “gap” near the outermost planet Neptune. This is because the azimuthal structure depends sensitively on the long-lived particles trapped in mean motion resonances with Neptune, and the times of residence in the various resonances are highly variable and unpredictable.

7. We have calculated disk brightness density and SEDs, assuming graybody absorption and emission from the dust grains. We find that the presence of planets modifies the shape of the SED. The solar system debris disk SED is particularly affected by the clearing of dust from the inner 10 AU because of gravitational scattering by Jupiter and Saturn.

8. Grain physical lifetimes are limited by collisions and sublimation. The comparison of the dynamical lifetime of particles, the timescale for structure formation, and the collisional time between KB and interstellar grains indicates that if the current estimates for the flux and the size distribution of interstellar grains are correct, collisional destruction is important for grains larger than about $6\ \mu\text{m}$. For smaller particles, debris disk structure will be able to survive,

although the smaller particles have less prominent structure associated with the outer planets. Depending on their composition, sublimation of particles may or may not play an important role in the destruction of structure. If KB dust has a water ice composition, and assuming a sublimation temperature of 100 K, it is likely that even large, $120\ \mu\text{m}$ particles will sublimate before reaching the inner 4 AU of the solar system. We conclude that grain destruction processes need to be examined more carefully in future applications of our studies to infer the presence of planets from structure in debris disks.

This work is part of the *SIRTF* FEPS Legacy project³ (principal investigator M. Meyer), with the goal “to establish the diversity of planetary architectures from SEDs capable of diagnosing the radial distribution of dust and the dynamical imprints of embedded giant planets.” The modeling of a particular system is very complex, because it

³ See <http://feeps.as.arizona.edu>.

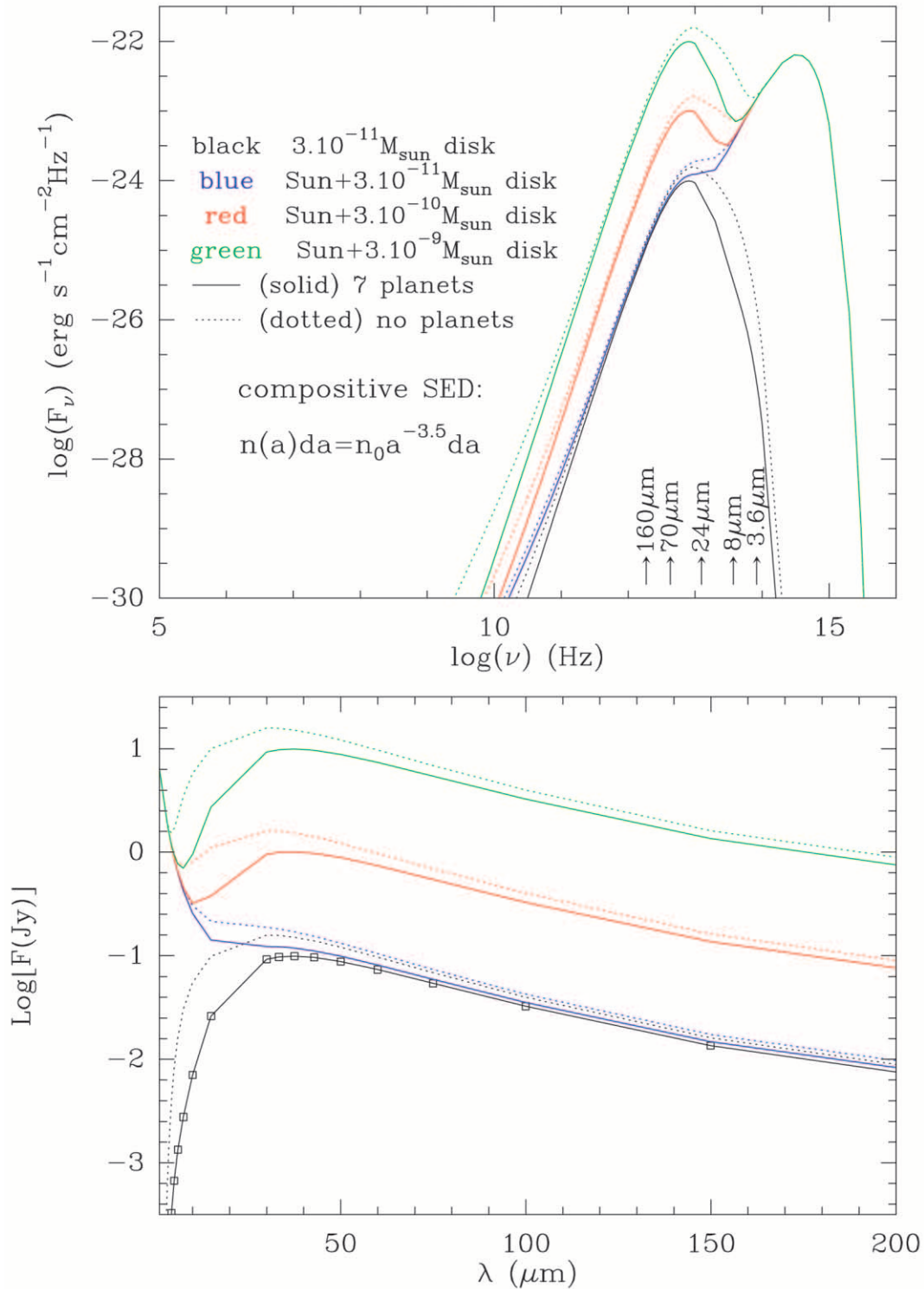


FIG. 14.—*Top*: Composite SEDs that result from combining the SEDs from the $\beta = 0.01, 0.05, 0.1, 0.2$, and 0.4 disks, with weights in such a way that they follow the size distribution $n(a) da = n_0 a^{-3.5} da$, where a is the particle radius. Black is for a $3 \times 10^{-11} M_\odot$ disk only; blue is for the Sun plus a $3 \times 10^{-11} M_\odot$ disk; red is for the Sun plus a $3 \times 10^{-10} M_\odot$ disk; and green is for the Sun plus a $3 \times 10^{-9} M_\odot$ disk. In all cases, the solid line is for a system with seven planets, the dotted line is for no planets, and the system is at a distance of 30 pc. *Bottom*: Same as above, but in janskys vs. microns. The squares correspond to the data points, indicating the spectral resolution on the synthetic SEDs.

involves a large number of free parameters. We have therefore chosen a forward modeling approach: a grid of models will be created for different planetary masses and orbital radii, parent bodies' masses and orbital distribution, total mass in dust particles, etc. We will produce dust spatial dis-

tributions like the ones presented here, which will be used as input for a radiative transfer calculation to generate SEDs containing all the important spectroscopic features. This will be more detailed than the simple graybody approximation used in the present work. This “library,” which as part

of our “Legacy” will be available to the community, will contain the templates to which we will compare the dust SEDs derived from the *SIRTF* observations for their interpretation in terms of planetary architectures.

We thank Hal Levison for providing the SKEEL computer code. A. M.-M. is supported by NASA contract 1224768, administered by JPL. R. M. is supported by NASA grants NAG 5-10343 and NAG 5-11661.

REFERENCES

- Backman, D. E., Dasgupta, A., & Stencel, R. E. 1995, *ApJ*, 450, L35
 Backman, D. E., & Paresce, F. 1993, in *Protostars and Planets III*, ed. E. H. Levy & J. I. Lunine (Tucson: Univ. Arizona Press), 1253
 Brown, M. E. 2001, *AJ*, 121, 2804
 Burns, J. A., Lamy, P. L., & Soter, S. 1979, *Icarus*, 40, 1
 Dermott, S. F., Durda, D. D., Gustafson, B. A. S., Jayaraman, S., Xu, Y. L., Gomes, R. S., & Nicholson, P. D. 1992, in *Asteroids, Comets, Meteors 1991*, ed. A. W. Harris & E. Bowell (Houston: Lunar Planet. Inst.), 153
 Duncan, M. J., Levison, H. F., & Lee, M. H. 1998, *AJ*, 116, 2067 (D98)
 Gustafson, B. A. S. 1994, *Annu. Rev. Earth Planet. Sci.*, 22, 553
 Jewitt, D. C., & Luu, J. X. 1995, *AJ*, 109, 1867
 Joswiak, D. J., Brownlee, D. E., Pepin, R. O., & Schlutter, D. J. 2000, in *Lunar and Planetary Science XXXI* (Houston: Lunar Planet. Inst.), 1500
 Kortenkamp, S. J., & Dermott, S. F. 1998, *Icarus*, 135, 469
 Liou, J.-C., Dermott, S. F., & Xu, Y.-L. 1995, *Planet. Space Sci.*, 43, 717
 Liou, J.-C., & Zook, H. A. 1997, *Icarus*, 128, 354
 ———. 1999, *AJ*, 118, 580 (LZ99)
 Liou, J.-C., Zook, H. A., & Dermott, S. F. 1996, *Icarus*, 124, 429 (LZD96)
 Liou, J.-C., Zook, H. A., & Jackson, A. A. 1999, *Icarus*, 141, 13
 Malhotra, R., Duncan, M. J., & Levison, H. F. 2000, *Protostars and Planets IV*, ed. V. Mannings, A. P. Boss, & S. S. Russell (Tucson: Univ. Arizona Press), 1231
 Stern, S. A. 1996, *A&A*, 310, 999
 Trujillo, C. A., & Brown, M. E. 2001, *ApJ*, 554, L95
 Wisdom, J., & Holman, M. 1991, *AJ*, 102, 1528
 Wyatt, S. P., Jr., & Whipple, F. L. 1950, *ApJ*, 111, 134
 Yamamoto, S., & Mukai, T. 1998, *A&A*, 329, 785
 Zook, H. A., & Berg, O. E. 1975, *Planet. Space Sci.*, 23, 183